Review of Scientific Instruments

Optical access to multi-anvil apparatus with ultrasonic method under high-pressure environment

Cite as: Rev. Sci. Instrum. **90**, 114502 (2019); https://doi.org/10.1063/1.5107438
Submitted: 29 April 2019 . Accepted: 02 November 2019 . Published Online: 20 November 2019

Qizhe Tang, Yonggang Liu, Wei Song, Xiang Chen, and Hongsen Xie

Review of Scientific Instruments ARTICLE scitation.org/journal/rsi

Optical access to multi-anvil apparatus with ultrasonic method under high-pressure environment

Cite as: Rev. Sci. Instrum. 90, 114502 (2019); doi: 10.1063/1.5107438
Submitted: 29 April 2019 • Accepted: 2 November 2019 •
Published Online: 20 November 2019

Qizhe Tang,[1,2] Yonggang Liu,[1,a)] Wei Song,[1] Xiang Chen,[1,2] and Hongsen Xie[1]

AFFILIATIONS

[1] Key Laboratory of High-Temperature and High-Pressure Study of the Earth's Interior, Institute of Geochemistry, Chinese Academy of Sciences, Guiyang 550081, China
[2] University of Chinese Academy of Sciences, Beijing 100049, China

[a)] **E-mail:** liuyonggang@vip.gyig.ac.cn

ABSTRACT

Optical methods have widely been utilized in high-pressure high-temperature experiments for the past several decades. However, optical investigations using the visible spectrum in large volume press have not been well explored. In this study, we incorporate optical access into a multianvil apparatus (MAA) to perform optical experiments. Furthermore, by acquiring the optical image of the sample under high pressure, we have realized the thickness measurement of the sample and further applied it to the existing ultrasonic measurement. We report the optical method from the aspects of apparatus modification, ruby scale, and the demonstrations of the feasibility of the optical access in the MAA.

I. INTRODUCTION

Optical experiments are of great importance in the study of materials in high-pressure geoscience, allowing us to directly view the sample during experiments. Until now, most optical experiments under high-pressure high temperature (HPHT) conditions have been carried out using diamond anvil cells (DACs) with great success. Notably, the transparent anvil makes the DAC a suitable optical experimental device, whose portability promotes ease of combination with synchrotron radiation and microscopes. The ease of combination in such devices permits physical parameters, such as Raman shift and X-ray diffraction, to be easily measured; moreover, so does direct observation of the sample. However, due to the oxidation of diamond at a high temperature, DAC generally does not work well above 850 °C (external heating), which greatly limits the research capability of DAC under HPHT conditions.[1,2]

In contrast, the multianvil apparatus (MAA) offers a quasihydrostatic environment with six anvils and is also used to generate high pressure in the laboratory. Despite the relatively lower pressure range compared with DAC, MAA works well at temperatures of up to 2000 °C or even higher, with small temperature gradients.[3] Another significant advantage of MAA is that the sample size is at least several orders of magnitude larger than in the DAC. Generally speaking, the larger the sample size, the easier it is to characterize its physical properties. Investigations of the physical properties of various minerals and rocks, such as their elastic, thermodynamic, and electrical properties, have been conducted extensively using MAA.[1] However, there has been little work conducted on the optical properties of minerals and rocks using the visible spectrum.

After decades of development, the technology of combining MAA with synchrotron radiation has matured (e.g., cubic-type[4–6] and Kawai-type[7]). For example, real-time image recordings in the MAA using X-ray radiography techniques have been possible for several years. With the aid of X-radiography, the viscosity of high-pressure liquid can be acquired using the falling-sphere method; sample length can be characterized precisely using X-ray imaging to calculate the acoustic velocity of the sample in conjunction with ultrasound, and the further phase-transformation point of mineral crystals at HPHT can be obtained using X-ray diffraction.[8] Nevertheless, even if combined with synchrotron radiation, *in situ* sample

observation in a MAA system is still not well explored using visible light.

In order to introduce the various optical techniques commonly used in the DAC system into MAA, to open a pathway for direct observation using visible light, there were several approaches for the direct visible light investigation of samples in the miniaturized multianvil pressure apparatus.[9–11] Visible light illuminates the sample through a small window on the upper anvil in a small numerical aperture, and great pressure on small samples at room temperature can be achieved. However, sample photographs taken during such experiments are not clear enough because of the small-aperture optical window. Benefitting from the large truncation anvil surface, we are able to establish a large aperture for an optical path in the MAA. In this paper, we report the establishment of optical access in a cubic multianvil apparatus, in which we achieved the *in situ* visible-light monitoring of the sample at pressures of up to 2.0 GPa and temperatures of up to 400 °C; the methodology was validated by ultrasonic measurements.

II. EXPERIMENTAL DESIGN

Experiments were carried out in the cubic anvil apparatus of YJ-3000T in the Key Laboratory for High-Temperature and High-Pressure Study of the Earth's Interior of the Institute of Geochemistry, Chinese Academy of Sciences.

The multianvil apparatus of YJ-3000T is a typical DIA-type cubic six-anvil apparatus, in which pressure is generated by compressing the sample volume with six tungsten carbide (WC) anvils, and is driven by a 3000-ton hydraulic pump. The apparatus uses 23.5 mm truncation edge length anvils and can heat the sample homogeneously in the vertical direction. To build in optical access, an axially tapered hole was made coaxially as the optical path in two horizontal anvils. As shown in Fig. 1(a), the WC anvil was penetrated by a tapered hole of 8.0 mm diameter, on the bottom, where the narrow, tapered hole ensured the stability of the optical path. As referred to by Kawazoe,[10] the tapered hole helps expand the numerical aperture (NA) of the optical access. Then, an inverted cone with a conical degree of 90.0 was used as a pedestal for the optical window, which was processed on the top end of the tapered hole on the anvil, as shown in Fig. 1(a).

The inverted cone on the anvil was used as the base of the optical window; thus, in order to match the base, we also made the optical window 90.0°. To achieve high precision in the 90° cone, we used a cylindrical grinder to process the optical-window material. The choice of high-pressure, optical-window material was synthetic single-crystal moissanite (purchased from Guangxi, China), according to the optical experiments from the work of Xu *et al.*,[12,13] and Okuchi *et al.*[14–18]

The moissanite crystals were pretreated before processing to increase their fracture strength. According to Matsunaga *et al.*,[19] the polycrystalline SiC is strengthened by heat treatment, and thus, it can be inferred that the strength in the low-fracture probability range of the moissanite can be dramatically improved after sintering in air for 24 h. Furthermore, we found that the quality of transparency of the heat-treated crystals was better than that of the unheated ones. The strengthened crystals were then processed into the frustum on the cylindrical grinder. As shown in Fig. 1(b), the conical degree of the frustum is 90.0°, which matches the pedestal on the anvil.

The moissanite optical window was glued onto the anvil with epoxy resin; the glue was strengthened by inorganic powder, creating a strong bond between the anvil and the crystal. After being

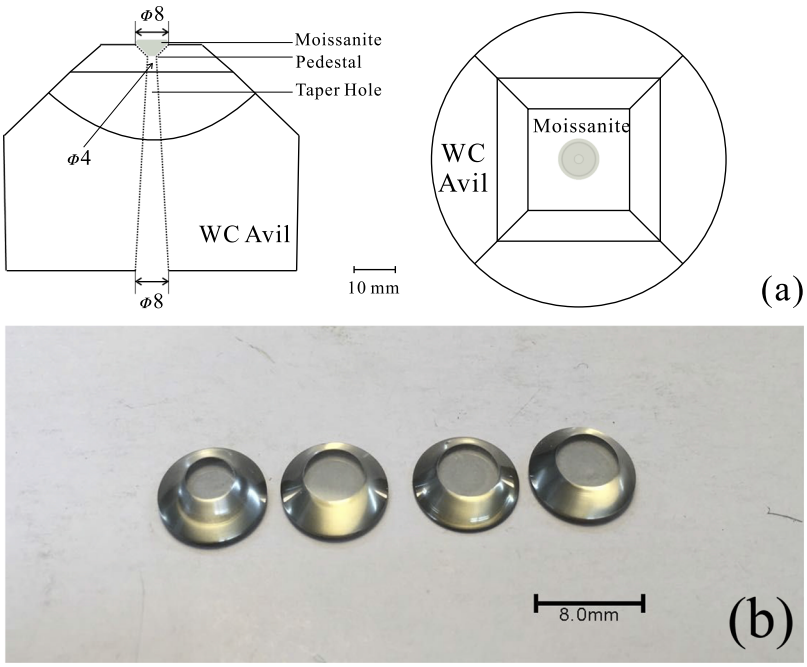

FIG. 1. (a) Side view (left) and top view (right) of the anvil. The pedestal of 90.0° on the anvil. (b) Set of 90.0° frustum moissanite crystals.

coupled to the optical high-pressure window, a set of aluminum-film mirrors was installed on the back of the anvil, as shown in Fig. 2(a), where the incident angle of the mirror and the light path is 22.5°. The structure of the MAA is so complicated that it is difficult to mount the light source on the optical access directly. Therefore, in order to minimize the structural deformation of the MAA, visible light must reflect several times before entering the sample chamber. In simple terms, light comes from the back of the MAA and is then focused and refracted before entering the sample chamber. As shown in the schematic diagram of Fig. 2(b), light enters the cell from behind through the holes on the steel sleeves and captured by the front camera; the laser beam is emitted by the excitation machine, exciting the

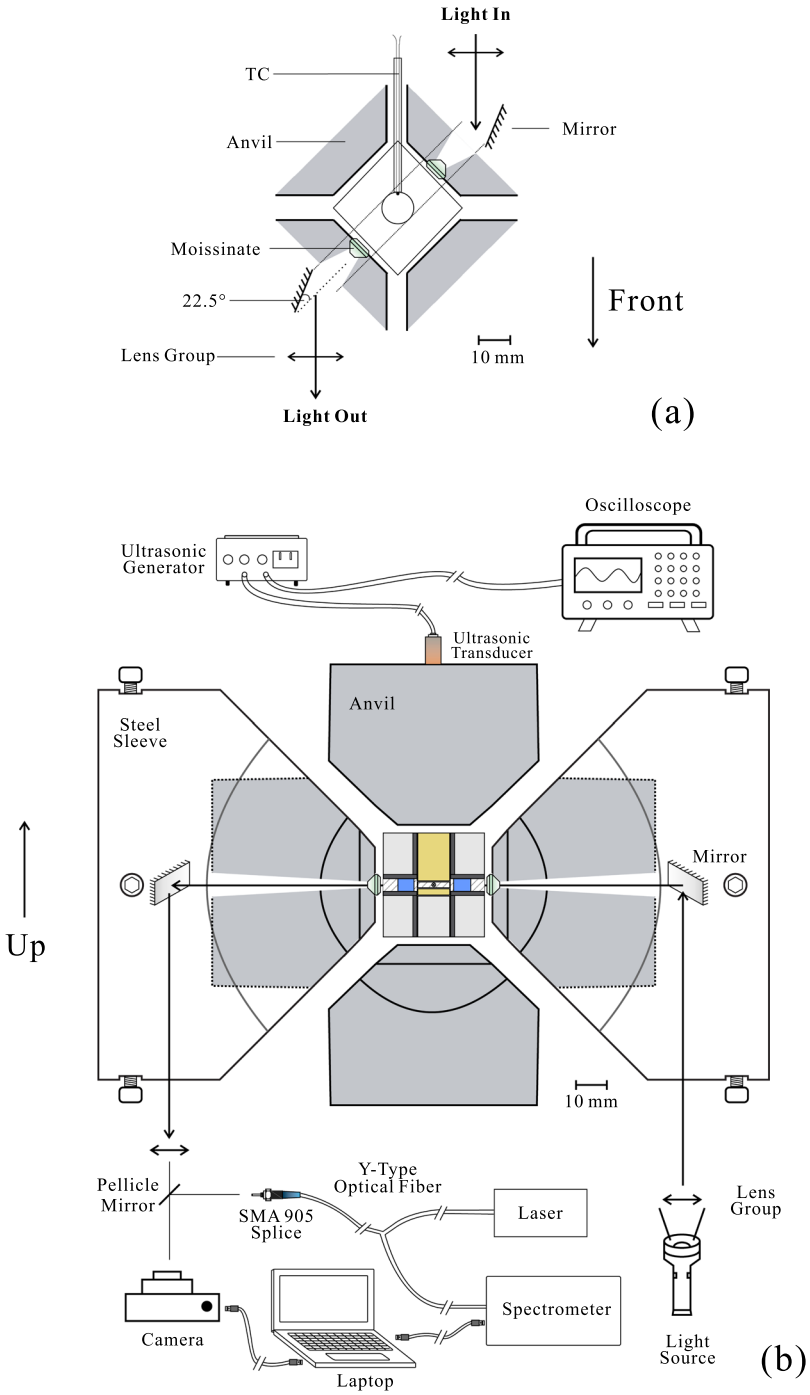

FIG. 2. (a) Top view of the working anvils. (b) Side view of the apparatus and the working components.

sample and generating the fluorescence signals, and is then received by the spectrometer on the same side. The camera and the Y-type optical fiber share one access; we used a SMA-905 splice to couple the lens group on the front side. With the aid of the lens group, holes, and mirrors, we were able to modify only minimally the original structure of the apparatus. Furthermore, a classical pulse-echo technique measurement system was installed in the vertical direction, and a longitudinal-wave ultrasonic transducer with 10 MHz center frequency, a digital oscilloscope (Tektronix DPO2024B, USA), and a CTS-8077PR ultrasonic pulse generator/receiver unit (Guangdong Goworld Co., Ltd., Shantou, China) were connected directly, as shown in Fig. 2(b).

III. TESTING

A. Sample assembly

The pyrophyllite cube ($33 \times 33 \times 33$ mm^3) with a vertical hole (Φ 12.0 mm) was used as a pressure-transmitting medium (PTM), which was installed with a graphite heating tube; a horizontal hole (Φ 6.0 mm) was used for optical access; and another hole (Φ 3.0 mm) was drilled on the back edge of the cube for thermocouples.

As shown in Fig. 3(a), an alumina ceramic buffer rod (Φ 8.0 mm, 14.0 mm length) is placed vertically on top for propagating ultrasonic signals. The sample is placed in the middle of the assembly, and another thinner (1.0 mm thickness) alumina ceramic rod is placed below the sample to enhance the acoustic impedance of the lower surface of the sample. An unsintered pyrophyllite buffer rod is placed at the bottom to maintain a vertically quasihydrostatic environment in conjunction with the above materials. The materials are then wrapped in a 1.0 mm thick graphite tube (10.0 mm outer diameter, 33.0 mm length) heater, in the center of which is a horizontal, penetrating hole (Φ 6.0 mm), drilled as part of the optical pathway.

Horizontally, the silica glass and finely ground NaCl powder are arranged in sequence, as shown in Fig. 3(a); both materials are enclosed tightly in graphite tubes (1.0 mm thickness) for transmitting visible light, but the tubes do not participate in the heating process. The fine and loose NaCl powder is adopted as the cushioning medium because it is barely fluorescent, has weak deliquescence, and most importantly, is transparent after compression.[20] A ruby sphere (Φ 1.0 mm) is embedded in the powder near the end of the sample; loose powder provides enough room for further compression, ensuring a hydrostatic environment along the optical path.

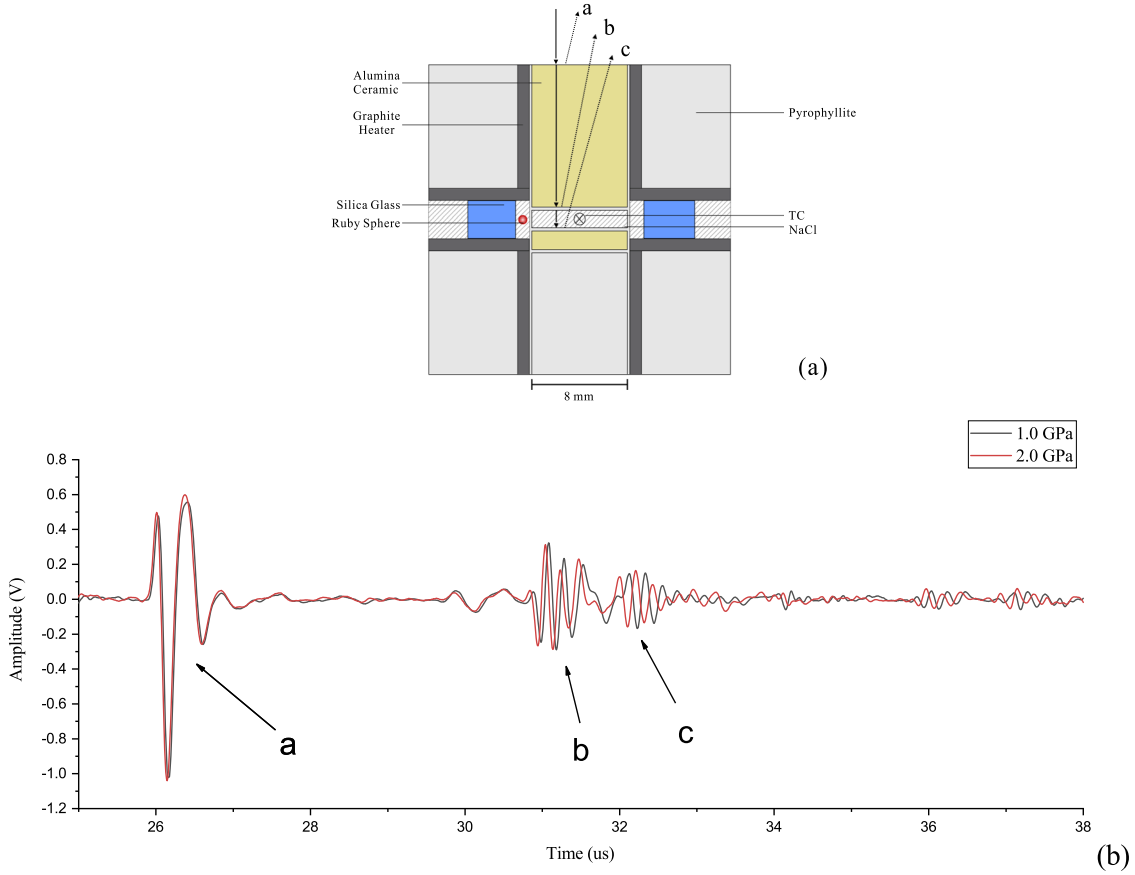

FIG. 3. (a) Schematic diagram of the sample assembly. The labels a, b, and c represent the ultrasonic reflected signals from the interfaces below. (b) A raw P-wave waveform of the acoustic signal, in which the interfaces a, b, and c are marked on the diagram. A significant offset occurs at the c position when the pressure reaches 2 GPa.

As shown in Fig. 2(b), the outside NaCl powder acts as a buffer for the optical window. During pressurization, the NaCl powder acts as spacer between the optical window and the silica glass. In addition, the type-K thermocouple (Ni-Cr and Ni-Si) contacts the sample edge directly from the rear.

B. Pressure calibration at room temperature

In addition to optical data, NaCl as a typical, transparent, geological sample provides complete elasticity data at HPHT. Therefore, on purpose, to make a comparison with previous work and to make full use of our improvements on the MAA, NaCl was the sample of choice in the experiments. First, NaCl powder was pressed into a disk of 8.0 mm diameter and 2.0 mm thickness; then, the disk was loaded into the assembly. During the pressurization experiments with an oil pressure interval of 2.0 MPa, the ruby fluorescent signals, the ultrasonic travel time of the sample, and the *in situ* photographs at different pressures were collected simultaneously.

The optical experiments began with optical pressure calibration. The main components and connections are demonstrated in Fig. 2(b): the sample end of the Y-type optical fiber was coupled to a telescope, and the other ends were connected to a 532 nm laser excitation device and a spectrometer (Flight Tech. Co., FLA 4000), respectively. The telescope contained a pellicle mirror, which provided us with a paraxial access for naked-eye observation. Through the telescope, the laser beam was focused to a small spot ($\Phi < 0.1$ mm) in the center of the ruby sphere. Ruby fluorescence signals were then collected and processed on the computer connected to the spectrometer. As shown in Fig. 4, the two fluorescence signals are obtained at room temperature under 1.0 GPa and 2.0 GPa.

The raw signals are strong enough to observe, and it is easy to obtain their FWHM.

Ruby is frequently used in DAC experiments for accurate pressure calibration, and according to previous studies,[21–24] using the ruby fluorescence peak shift under hydrostatic conditions is a reliable way to derive the pressure. Therefore, the actual pressures in this study were also derived by the shift of the R2-peak of the ruby fluorescence. The pressure conversion formula,[25] which is used to calibrate pressure in the MAA, is

$$P = A/B[1 + (\Delta\lambda/\lambda_0)]^B - 1, \quad (1)$$

where P is the pressure in megabar, and λ and λ_0 are the real-time wavelength of the ruby R-line and the 1-bar wavelength, respectively. A and B are constants, where $A = 19.04$ and $B = 7.665$.

C. Cross-validation: Manganin wire pressure calibration

The YJ-3000T cubic anvil apparatus was calibrated using the fix-point method with bismuth, NaCl, KCl, and LiCl, which gave a reliable calibration curve. In order to verify the reliability of our optical measurement system, a section of data in the room temperature range of low-pressure (less than 3 GPa) on the curve is intercepted for cross-validation. At room temperature, the pressure was calibrated by the resistance of a manganin wire,[26–28] using the formula proposed by Fujioka *et al.*; pressure is linearly related to resistance and, finally, seamlessly connected with the first phase transition point of bismuth. Therefore, the manganin wire calibration curve in the standard assembly is used for comparison with the ruby gauge calibrated within the optical system. This kind of cubic press routinely has the potential to produce high pressures up to ~5–6 GPa within its first stage of compression, but to protect the gems and the holed WC anvils, the maximum pressure in the experiments was not allowed to exceed 3 GPa.

In Fig. 5, the two curves represent the optical pressure calibration (black) and the manganin wire calibration (red) results, whose slopes are 1.54 and 1.44, respectively, with an obvious offset between the two curves. In contrast with the optical assemblies, the manganin wire calibration was carried out in a standard assembly without an optical path. Therefore, it is the dissimilarity between the assemblies that produces the offset shown in Fig. 5, giving them different initial

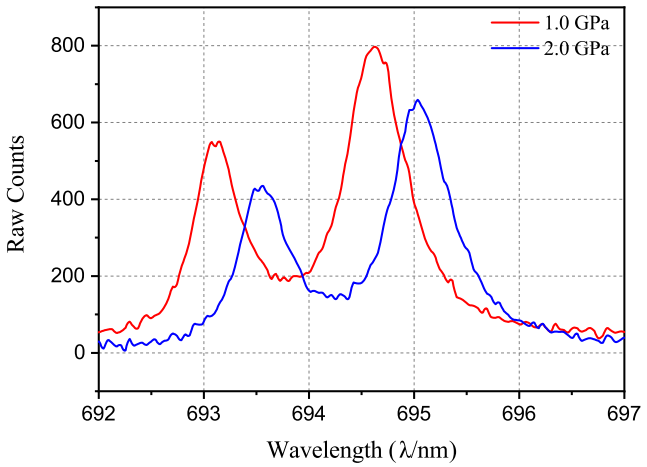

FIG. 4. Ruby fluorescent signals at 1.0 GPa and 2.0 GPa, showing 0.44 nm peak shift at the full width half maximum (FWHM) of the R2-line of the two spectra.

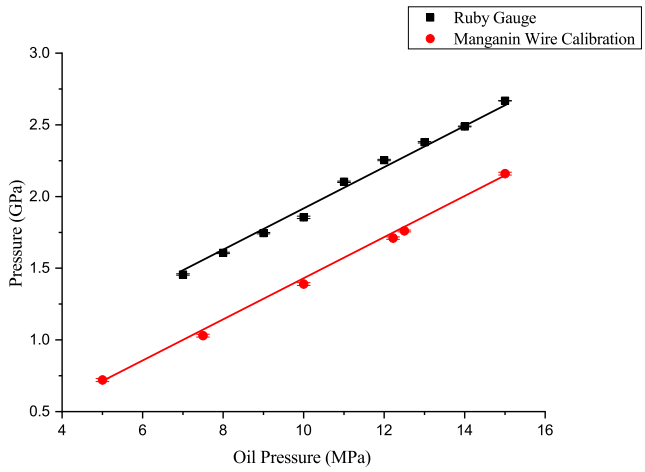

FIG. 5. Comparison of ruby calibration and fix-point calibration: black squares for optical calibration (1.53 for its fitted curve slope) and the red curve for fix-point pressure calibration (1.43 for its slope).

values but almost-matching increments. In other words, the offset proves the feasibility of using a ruby scale in a cubic anvil apparatus. Similar pressure increments prove the high sensitivity and accuracy of the ruby scale, even within a relatively low-pressure range.

D. High temperatures

We also attempted high temperature calibration using ruby fluorescence in the same apparatus. Unfortunately, ruby is not a suitable material for pressure calibration at high temperature. When Barnett[22] first used ruby to calibrate pressure in the DAC, it was found that ruby's sensitivity to high temperature made it unsuitable, even though alumina is an ideal secondary calibration material under high pressure. The same results were reproduced in our experiments. As shown in Fig. 6, the two peaks of the ruby fluorescence spectrum are used for pressure calibration. However, with rising temperature, the peaks gradually decrease in intensity and overlap and are ultimately not able to be distinguished at 400 °C.

Ruby fluorescence varies with pressure at a high temperature, as seen in Fig. 6, but the ruby scale is still unable to calibrate pressure at a high temperature due to the lack of a proper temperature correction method. In addition, the transparent sample is further compacted with increasing pressure, making *in situ* photographs clearer under higher pressure, but when the temperature starts to rise (up to 400 °C), the photographs dim and their clarity diminishes. We observed a leakage of graphite in the sample assembly after pressure relief, turning the NaCl disk dark. Consequently, the sample contamination made it difficult to identify the boundaries during *in situ* thickness measurement. The sample assembly thus needs to be improved to prevent vertical graphite leakage during the heating process.

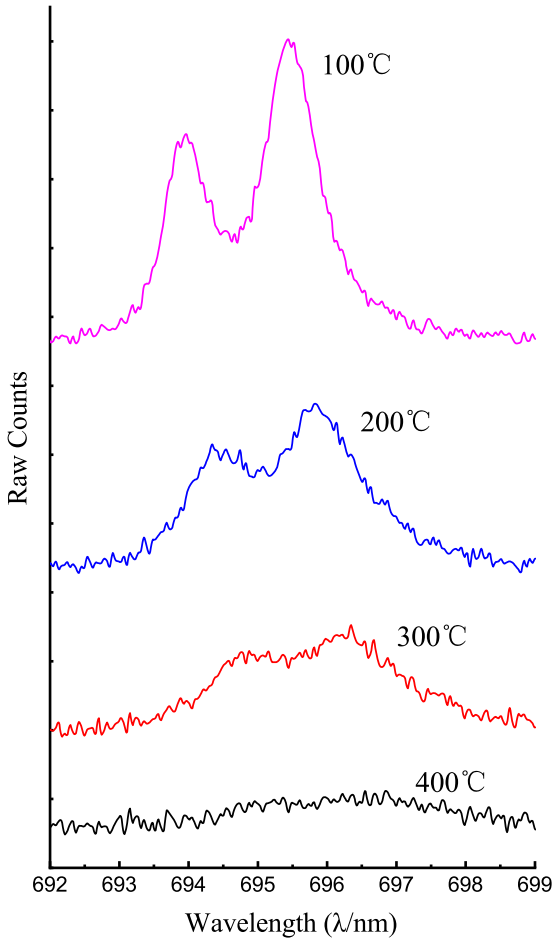

FIG. 6. Spectrum of ruby fluorescence at 2 GPa. Curves from the top to bottom are 100 °C, 200 °C, 300 °C, and 400 °C.

IV. VALIDATION—NaCl VELOCITY MEASUREMENT

During an ultrasonic velocity measurement, the values of the thickness of a sample under high pressure are crucial for velocity calculation. In this work, the *in situ* photographs of the sample at each pressure were used for thickness measurement to calculate the *in situ* sound velocity of the NaCl sample. Then, the sound velocity–pressure curve was plotted and compared with the results from previous studies.

In sample thickness measurement, the principle of linear propagation of light is adopted. With increasing pressure, the sample was illuminated by the light source from the rear, and the light was obstructed by the opaque alumina ceramics on the upper and lower surfaces of the sample, creating a light band in the photographs. Moreover, the ruby sphere near the sample became a reliable length scale during thickness measurement as we found that sphere's shape remained barely unchanged after pressure relief.

As shown in Fig. 7, line AB comes from the greatest brightness change area in the light band, which is extracted from the photograph and transformed into grayscale, shown as the brightness curve on the left side of Fig. 7. The fastest changes in the curve correspond to the upper and lower edges of the light band. Additionally, the irregular shadow in the center of the light band is also reflected as a sharp decline in the brightness curve, which corresponds to the break in the optical high-pressure window in the pressurization process. So, using the diameter of the ruby sphere, the *in situ* thickness of the sample is calculated by measuring the pixel length between the upper and lower edges of the light band on the photograph.

Next, the *in situ* ultrasonic travel time is analyzed by using the pulse-echo method.[29–33] As shown in Fig. 3(b), we obtained the time intervals between interfaces a, b, and c, so the two-way travel time and the sound velocity of the sample could be calculated by subtracting the reflection time of the two interfaces from the whole propagation time. As shown in Fig. 8, we present the results by Matsui *et al.*, for comparison.[34] The data errors in the figure originated from measuring thickness and travel time; after error transmission, errors are illustrated in the diagram with the maximum value not exceeding 2.0%.

Evidently, the experimental results obviously fluctuate around the red curve, as shown in Fig. 8. Judging from the experimental data, our fitting results are similar to those of Matsui *et al.* Even though our fitting coefficients are relatively poor, good agreement exists between both sets of results. The fluctuations are probably due to an insufficient number of pressure values and the dimness of the *in situ* photographs. In other words, the accumulation

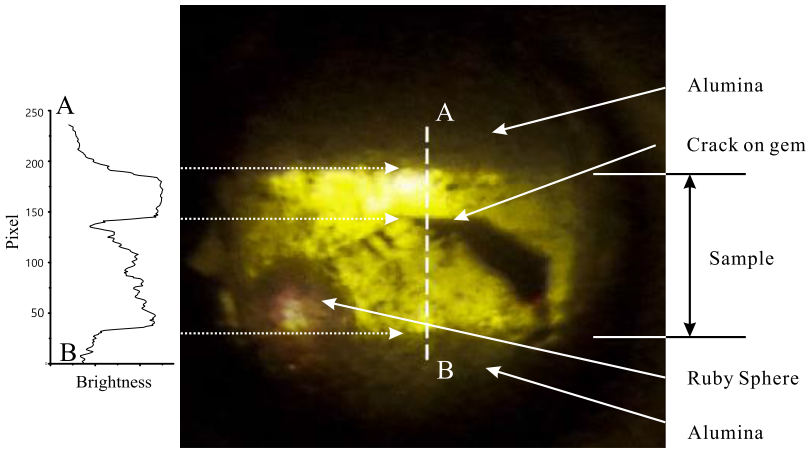

FIG. 7. Diagram of thickness measurement: brightness curve on the left, ruby sphere as a length scale of 1.0 mm diameter.

and transmission of uncertainty during thickness measurements are important factors leading to the instability of the sound–velocity measurement.

In our thickness measurement, sample length was obtained using the distance between the upper and lower boundaries from the *in situ* photographs of the sample, shown in Fig. 7. In previous studies, sample length was derived by the internal consistency method developed by Cook[35] that used both P waves and S waves together. With this approach, Li *et al.*[36] used the interferometry method and measured the sound velocity of the sample successfully. Later, synchrotron radiation and X-ray imaging technology led to a better way to measure the length of the sample under high pressures.[5,34,37] In the above research, measurement accuracy becomes increasingly important for acquiring the high pressure sound velocity. Therefore, our study shows that, once our photo resolution gets an upgrade, the use of visible-light imaging to measure sample length is expected to hold great potential for wide applications, which is also an important motivation of our study.

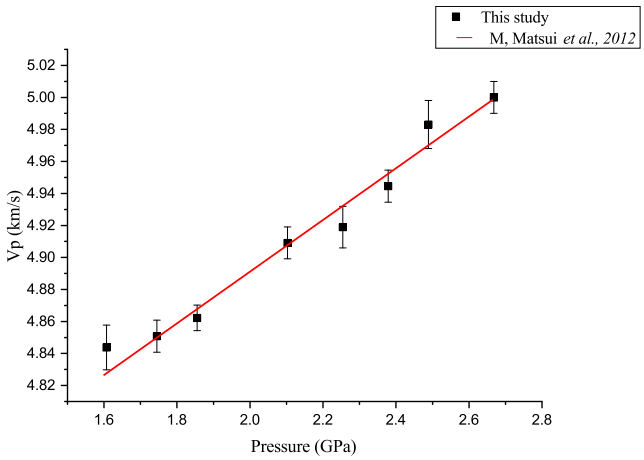

FIG. 8. Comparison results of sound velocity–pressure curves: black squares for our results and the red curve for the results of Matsui *et al.*

V. CONCLUSION

Through a series of optical experiments, the feasibility of the optical access to MAA has been verified. From the results of validation experiments, we have preliminarily achieved the real-time monitoring of samples in a cubic anvil apparatus, including the *in situ* observation of samples and the real-time pressure determination inside the sample chamber. The experimental platform that we built requires refinement that we intend to carry out in the next experimental phase, which when optimizing the sample assembly to accurately measure sound velocity at a high-temperature will be a priority. However, compared with previous studies, the combination of optical experiments and the ultrasonic method in the MAA is only a preliminary application. We intend to combine more sophisticated optical methods with our cubic anvil apparatus, such as the Raman spectrometer, infrared spectrometer, and optical pyrometer. Furthermore, the key significance of the optical experiments involving the MAA is that once visible and optical spectroscopy are introduced to the high-pressure device, the data of *in situ* structural change, morphology, and phase transformation can be obtained in a more reliable and direct way.

ACKNOWLEDGMENTS

This work was supported by the National Natural Science Foundation of China (Grant No. 41873075). We also thank Dr. Wenge Zhou at the Institute of Geochemistry in Chinese Academy of Sciences for technical support and helpful discussions.

REFERENCES

[1] A. Jayaraman, Rev. Mod. Phys. **55**(1), 65–108 (1983).
[2] A. Jayaraman, Rev. Sci. Instrum. **57**(6), 1013–1031 (1986).
[3] J. Osugi, K. Shimizu, K. Inoue, and K. Yasunami, Rev. Phys. Chem. Jpn. **34**(1), 1–6 (1964).
[4] B. Li, M. Vaughan, J. Kung, and D. Weidner, NSLS Activity Report, Vol. 2, pp. 103–106, 2001; available at https://www.bnl.gov/isd/documents/23813/section%202/science_highlights.htm.
[5] B. Li, J. Kung, and R. C. Liebermann, Phys. Earth Planet. Inter. **143-144**, 559–574 (2004).

[6]T. Yagi, Y. Ida, Y. Sato, and S.-I. Akimoto, Phys. Earth Planet. Inter. **10**(4), 348–354 (1975).
[7]Y. Higo, T. Irifune, and K. I. Funakoshi, Rev. Sci. Instrum. **89**(1), 014501 (2018).
[8]T. Irifune, N. Nishiyama, K. Kuroda, T. Inoue, M. Isshiki, W. Utsumi, K.-i. Funakoshi, S. Urakawa, T. Uchida, and T. Katsura, Science **279**(5357), 1698–1700 (1998).
[9]Z. Wang, D. He, W. Zhang, W. Li, W. Li, J. Qin, L. Lei, Y. Zou, and X. Yang, Rev. Sci. Instrum. **81**(8), 085102 (2010).
[10]T. Kawazoe, Rev. Sci. Instrum. **83**(3), 035111 (2012).
[11]E. Sterer and I. F. Silvera, Rev. Sci. Instrum. **77**(11), 115105 (2006).
[12]J.-a. Xu and H.-k. Mao, Science **290**(5492), 783–785 (2000).
[13]J.-a. Xu, H.-k. Mao, R. J. Hemley, and E. Hines, J. Phys.: Condens. Matter **14**(44), 11543 (2002).
[14]T. Kimura, N. Ozaki, T. Okuchi, T. Terai, T. Sano, K. Shimizu, T. Sano, M. Koenig, A. Hirose, and T. Kakeshita, Phys. Plasmas **17**(5), 054502 (2010).
[15]T. Okuchi, S. Sasaki, T. Osakabe, Y. Ohno, S. Odake, and H. Kagi, in *International Conference on High Pressure Science and Technology, Joint AIRAPT-22 and HPCJ-50*, edited by K. Takemura (IOP Publish Ltd., 2010), Vol. 215.
[16]T. Okuchi, S. Sasaki, Y. Ohno, J. Abe, H. Arima, T. Osakabe, T. Hattori, A. Sano-Furukawa, K. Komatsu, H. Kagi, W. Utsumi, S. Harjo, T. Ito, and K. Aizawa, in *23rd International Conference on High Pressure Science and Technology*, edited by S. C. Gupta (IOP Publish Ltd., 2012), Vol. 377.
[17]T. Okuchi, N. Tomioka, N. Purevjav, J. Abe, S. Harjo, and W. Gong, High Pressure Res. **34**(2), 273–280 (2014).
[18]T. Okuchi, M. Yoshida, Y. Ohno, N. Tomioka, N. Purevjav, T. Osakabe, S. Harjo, J. Abe, K. Aizawa, and S. Sasaki, High Pressure Res. **33**(4), 777–786 (2013).
[19]N. Matsunaga, K. Nakahama, Y. Hirata, and S. Sameshima, J. Ceramic Process. Res. **10**(3), 319–324 (2009).
[20]R. H. Wentorf, *Modern Very High Pressure Techniques* (Butterworths, 1962).
[21]R. A. Forman, G. J. Piermarini, J. D. Barnett, and S. Block, Science **176**(4032), 284–285 (1972).
[22]J. D. Barnett, S. Block, and G. J. Piermarini, Rev. Sci. Instrum. **44**(1), 1–9 (1973).
[23]G. J. Piermarini, S. Block, J. D. Barnett, and R. A. Forman, J. Appl. Phys. **46**(6), 2774–2780 (1975).
[24]H.-K. Mao and P. M. Bell, Science **191**(4229), 851–852 (1976).
[25]H. K. Mao, J. Xu, and P. M. Bell, J. Geophys. Res.: Solid Earth **91**(B5), 4673–4676, https://doi.org/10.1029/jb091ib05p04673 (1986).
[26]N. Fujioka, O. Mishima, S. Endo, and N. Kawai, J. Appl. Phys. **49**(9), 4830–4832 (1978).
[27]J. Zhang, Z. Kou, D. He, F. Wang, X. Chen, Y. Zhang, Y. Li, and W. Hongru, Tool Eng. **43**(4), 18 (2009).
[28]H. Yongxiang, J. Seismol. Res. **7**(2), 209–216 (1984).
[29]H. B. Huntington, Phys. Rev. **72**(4), 321–331 (1947).
[30]H. J. McSkimin, J. Acoust. Soc. Am. **22**(4), 413–418 (1950).
[31]H. J. Mcskimin, J. Appl. Phys. **24**(8), 988–997 (1953).
[32]H. J. Mcskimin, J. Acoust. Soc. Am. **33**(1), 12–16 (1961).
[33]H. J. Mcskimin and P. Andreatch, J. Acoust. Soc. Am. **41**, 1052–1057 (1967).
[34]M. Matsui, Y. Higo, Y. Okamoto, T. Irifune, and K.-I. Funakoshi, Am. Mineral. **97**(10), 1670–1675 (2012).
[35]R. K. Cook, J. Acoust. Soc. Am. **29**(4), 445–449 (1957).
[36]B. Li, I. Jackson, T. Gasparik, and R. C. Liebermann, Phys. Earth Planet. Inter. **98**(1-2), 79–91 (1996).
[37]X. Wang, T. Chen, X. Qi, Y. Zou, J. Kung, T. Yu, Y. Wang, R. C. Liebermann, and B. Li, J. Appl. Phys. **118**(6), 065901 (2015).